GG2: CT Reconstruction and Visualisation
Interim Report

Sanchit Gandhi
Group 1
CRSiD: sg836
Queens' College

May 21, 2020

1   Introduction

This report documents the first half of the X-ray Computed Tomography (CT) Reconstruction and Visualisation project, in which a functional CT simulator was developed. Starting from the generation of X-rays, to modelling the operation of clinical CT devices and the principles of image reconstruction, the CT simulator covers the entire data acquisition process and generates a 2D image from the recordings made. Throughout the project, the simulator was used to investigate key scanning and reconstruction properties and the impact they have on the reconstructed image.

2   X-ray Generation, Scattering and Detection

X-rays are short-wave electromagnetic radiation, defined as having wavelengths in the range 0.01 to 1 nm [4]. The wavelength λ and energy E are related by $E = \frac{hc}{\lambda}$, where h is Planck's constant and c the speed of light. Having such short wavelengths, X-ray energies are very high, varying from 1.2 to 124 keV. As a comparison, visible light has a typical photon energy of 2.5 eV, of the order of 10^5 times smaller. It is the high energy property of X-rays which makes them useful for medical imaging- their high energy and momentum allows them to penetrate through patients, such that a projection image can be formed.

An *X-ray tube* is used to produce the X-rays which are transmitted to the patient [10]. A cathode element is heated, causing it to emit electrons via *thermionic emission*. These electrons are accelerated across a potential difference towards the anode, which is typically constructed of metal with a high melting point and continuously rotated to prevent it melting. As the electrons strike the anode, they interact with the nuclear field of the target atoms, causing them to deviate from their original trajectories with lower velocities. The reduction in kinetic energy is radiated as a photon with equal energy. Photons generated through this process are *polyenergetic* and are termed *Bremsstrahlung* or *braking radiation*. Bremsstrahlung gives a continuous distribution of X-ray energies, with additional discrete peaks at energies specific to the element due to *characteristic radiation*.

The amount of X-ray radiation delivered to a patient is typically quoted as a 'dose', in terms of the product of an amplitude and time quantity. The minimum dose is required is a tradeoff between two factors: increasing the dose improves the signal-to-noise ratio (SNR) of the CT image, however this is at the expense of greater patient radiation exposure.

X-rays *ionize* material in several different ways, interacting with matter to eject electrons [12]. There are two such mechanisms relevant to medical imaging, both of which lead to a reduction in X-ray energy. *Compton scattering* is the phenomenon by which an incoming X-ray photon collides with and transfers part of its energy to a weakly bound, outer shell electron. The electron escapes with some kinetic energy, and the X-ray photon is scattered in a random direction with lower energy. For low-to-mid energy incident photons, the scatter distribution is fairly isotropic, becoming more forward dominated as the energy is increased [9]. *Photoelectric absorption* occurs for the case where the incident energy of the X-ray photon exceeds that of the binding energy of the inner shell electron it interacts with [4]. The photon is completely absorbed and the electron ejected from the atom. The resultant core vacancy is filled by an electron which *relaxes* from a higher shell, which in turn

emits a photon of energy equal to the energy difference between the two levels. Since the energy of this emission depends on the initial and final electron energy levels, which are specific to each element, the distribution of the radiation is *characteristic* of the element.

The attenuation of a monoenergetic X-ray beam passing through a homogeneous medium follows an exponential distribution, with exponent given by the *linear attenuation coefficient* μ:

$$I = I_0 e^{-\mu x} \tag{1}$$

where I_0 is the intensity of the incident beam, I the intensity of the outgoing beam and x the thickness of material [12]. The value of μ is dependent on the photon energy E, atomic number Z and density of the material ρ. These dependencies are characterised for each attenuation mechanism: for Compton scattering $\mu \propto \frac{\rho}{E}$, whilst for the photoelectric effect $\mu \propto \frac{\rho}{E^3}$. Photoelectric interactions are more probable in higher density materials, as electron binding energies tend to be closer to photon energies, increasing the chance of complete electron ejection [11]. Fig. 1 is a logarithmic plot of μ as a function of E for several different materials. This data confirms the linear dependence of μ with material density, the linear attenuation coefficients scaling with ρ for constant photon energies. The dashed annotations for air and bone demonstrate that μ decreases at a constant rate of -3 for lower photon energies, transitioning to a smaller constant rate of -1 at higher photon energies. This implies that the photoelectric effect is the dominant attenuation mechanism at low energies, typically those less than 0.01 MeV, and Compton scattering for higher energies, those above 0.2 MeV.
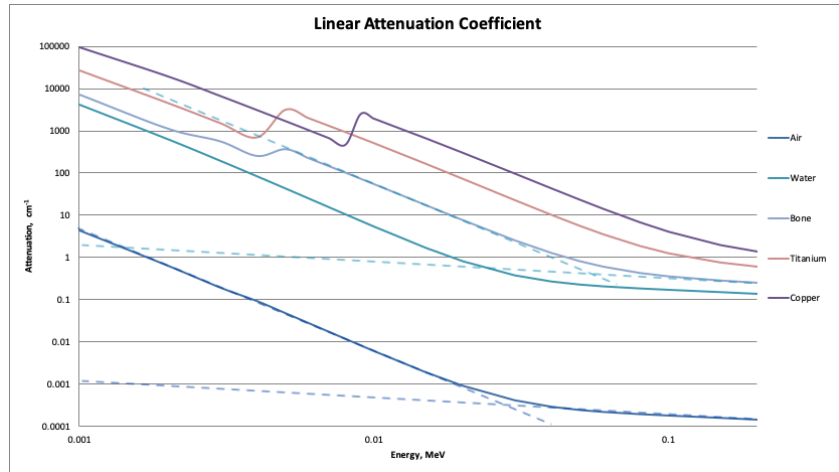

Figure 1: Variation of linear attenuation coefficient with energy for a range of materials.

The size of the transition region also varies with material density, with larger transition bands for higher density materials. This result is highlighted in Table 1, which records the transition range alongside density for the five materials investigated.

Table 1: Energy limits and transition region for each attenuation mechanism for various materials.

Material	Density (g/cm3)	Photoelectric upper limit (MeV)	Compton lower limit (MeV)	Transition range (MeV)
Air	0.00121	0.015	0.040	0.025
Water	1.00	0.020	0.060	0.040
Bone	1.92	0.035	0.100	0.065
Titanium	4.54	0.060	0.12	0.065
Copper	8.96	0.080	0.12	0.065

Presuming a discrete energy distribution of X-rays passed through a set of homogeneous materials, as is the case with the developed simulator, the intensity of the outgoing beam is found as a summation over beam

2

energies E and materials m:

$$I_{\text{tot}} = \sum_E I_{0,E} e^{-\sum_m \mu_{m,E} x_m} \tag{2}$$

where $\mu_{m,E}$ is the linear attenuation coefficient for material m at photon energy E. The intensity of the outgoing X-ray beam is typically measured through the use of a *scintillation counter* [7]. This device consists of a *scintillator*, which produces flashes of visible light as X-rays are absorbed by Compton scattering and photoelectric absorption, coupled to a *photocathode*. The light which strikes the photocathode causes it to emit electrons, the number of which is amplified through a series of dynodes. The device outputs a current with amplitude proportional to the energy of the incoming X-ray photon. As X-rays propagate through the object being imaged, they may be deviate in trajectory as they interact with atoms through Compton scattering. X-rays which reach the detector at large scatter angles diminish the image quality. To overcome this, a grid of hollow, cylindrical objects called *collimators* are placed in front of the scintillator [2]. They are typically made of lead, or a material with a similarly high distribution of linear attenuation coefficients, such that scattered X-rays are absorbed before reaching the detector.

The first task in developing the CT simulator involved completing the function `attenuate` to return residual beam intensities at specified depths for a set of input photon energies and material linear attenuation coefficients. This was achieved by taking the outer product of the coefficient and depth arrays to give a matrix with entries corresponding to the exponent of eq. (1). The residual intensities were then found by taking the element-wise product with the incident energy input array.

The function `ct_detect` implements eq. (2) to yield the total residual energy for a set of materials at different depths. For each material in turn, `attenuate` is called to produce a 2D array of residual energies and corresponding samples. Summing over all energies gives the total residual energy for all possible propagation paths from the source, through the various materials, to the given depths.

The variation of residual beam intensity with depth through five materials was investigated through use of the `ct_detect` function, the results of which are shown on a logarithmic scale for beam intensity in Fig. 2. Two different source energies were used: the 'ideal' source was generated by the `fake_source` function to produce the results of Fig. 2a, whereas 'source photon' was obtained from the `source` class to yield the distribution shown in Fig. 2b. Details regarding the implementation and distribution of each source can be found in Section 3.2 of the project handout.
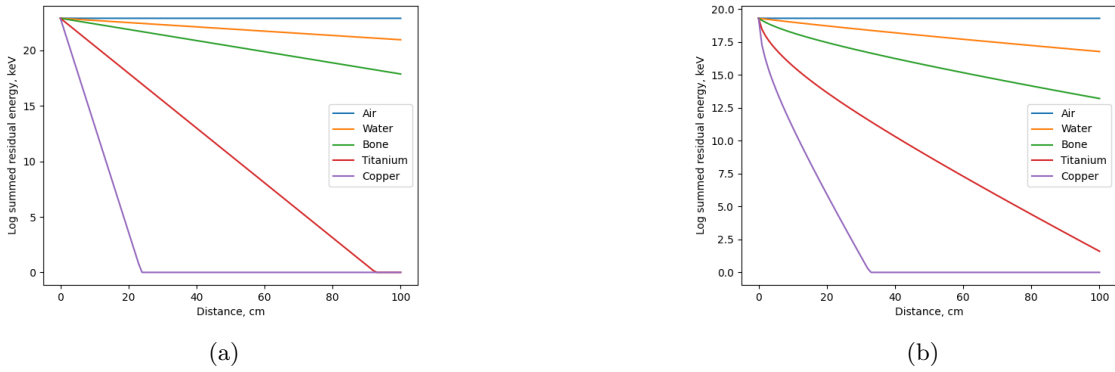

(a)

(b)

Figure 2: Variation of the logarithm of residual energy with distance for different materials. (a) 'Ideal' 100 kVp photon energy source. (b) 100kVp `source` photon energy distribution with a 2mm Al filter.

Taking the logarithm of both sides of eq. 1 yields:

$$\ln I = \ln I_0 - \mu x \tag{3}$$

which is in the form of a straight line with gradient $-\mu$ and y-intercept $\ln I_0$. The 'ideal' source is monoenergetic, and so the linear attenuation coefficient takes a single value corresponding to the single energy present. Hence, the logarithm of the residual beam intensity follows eq. (3), yielding straight lines as in Fig. 2a. For the cases of copper and titanium, the materials of the five investigated with the greatest linear attenuation coefficients, the lines level out at 25 cm and 90 cm, corresponding to the points at which point the entire X-rays are attenuated to 0 energy.

3

On the other hand, the `source` distribution is polyenergetic, comprising of a range of photon energies, such that each material takes a range of linear attenuation coefficients. As a result, the logarithm of residual intensities do not vary linearly with distance, giving curves instead of straight lines. The gradients are steepest at smaller distances, becoming shallower with increased penetration depth. This phenomenon, called *beam hardening*, occurs as a result of lower energy radiation getting attenuated faster than higher energy radiation, as the linear attenuation coefficient is greater for lower energy radiation. Hence, as the beam propagates through the material the proportion of high energy radiation increases, which in turn is attenuated to a lesser degree.

3   CT Scanning and the Sinogram

Cross-sectional CT images are formed by passing X-rays through an object over a number of offsets r and angles θ. 1st generation CT, as modelled by the developed CT simulator, achieves this with a single X-ray tube and detector. The source is collimated to produce a thin, directed X-ray beam, which is translated across the patient in discrete intervals to form a set of parallel projections. Both source and detector are then rotated by a fixed angle, and a subsequent set of projections obtained. This process is repeated over many angles, giving line attenuation measurements over the entire cross-section of the subject. The evolution of CT scanners and their operations are shown in Fig. 3. Using 2D imaging techniques, *sequential CT* can be used to produce full 3D images by scanning a plane, shifting the subject and scanning the next plane.
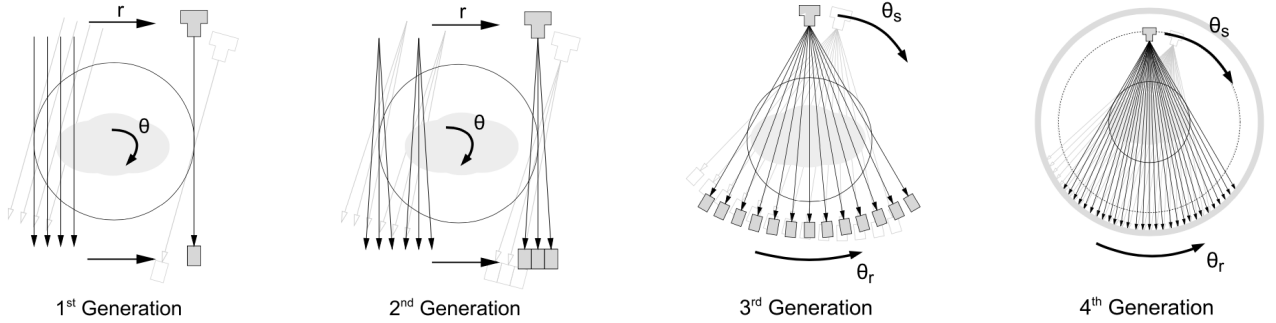

Figure 3: CT Generations. 1st gen: single-beam single-detector, translate-rotate motion. 2nd gen: fan-shaped beam and numerous detectors, translate-rotate motion. 3rd gen: fan-shaped beam and detectors arranged in an arc, translate-roate motion. 4th gen: fan-shaped beam and detectors mounted along a fixed outer ring, rotation only.

For a given scan angle θ, the set of parallel X-ray beams will not necessarily be aligned with the grid of pixels that form the subject (or 'phantom') image. *Interpolation* is the process of generating data values at any given point from the original phantom 2D array, such that a set of material data aligned with the X-rays can be formed. Interpolated data takes the value of the original data at the sampling points, as a pose to approximated data which in general does not.

Nearest neighbour is an interpolation method in which the value of the reslice pixel is taken to be that of the closest slice. It is, therefore, a discontinuous interpolation method, as the pixel intensities vary step-wise in value, giving rise to step artifacts in the output image. Interpolants which take the form of piecewise polynomials are termed *splines*. *Linear interpolation* is a spline scheme which sets the interpolated pixel value as a weighted sum of the data pixels on the two neighbouring slices. Hence, the reslice pixel data varies continuously in value (G^0 continuity). Using third-degree polynomials to give a *cubic* interpolation of the data points is particularly powerful, as geometric and parametric properties can be controlled through choice of the four polynomial coefficients, without introducing significant overfitting, an issue which occurs for polynomials of a higher order.

The `ct_phantom` function generates a phantom image, outputting a 2D square array of specified dimension with values corresponding to the material present at a given index. A number of different image configurations are specified, some of which have distinct features and properties, allowing for different aspects of the CT simulator to be tested in turn.

A generated phantom can then be scanned over a given number of angles using the `ct_scan` function to produce a sinogram. At each scan angle, the phantom array is interpolated to yield a 2D data array aligned with

the scan direction, and the amount of each material along each X-ray line calculated. Having scaled the amount of material by the resolution of the phantom image, the outgoing attenuated beam energy is found by calling the `ct_detect` function for each material in turn. Linear interpolation of the phantom image is implemented through use of the `ndimage.map_coordinates` scheme from the SciPy library.

Varying the number of angles over which a phantom is scanned has a significant impact on the resulting sinogram. A phantom comprised of a single large titanium hip replacement was scanned using 64, 128, 256 and 512 angles in turn. Magnified sections of the raw sinograms are shown in Fig. 4. The resolution of the sinogram improves with number of scanning angles: as the number of projections is increased, the number of rows in the discretised sinogram increases. An increase in the number of data points results in a reduction in the scale of block artifacts. A quantitative assessment of the impact of scanning angles on the CT simulation process is provided in Section 4, in which the accuracy of the reconstructed image is compared to the original phantom.
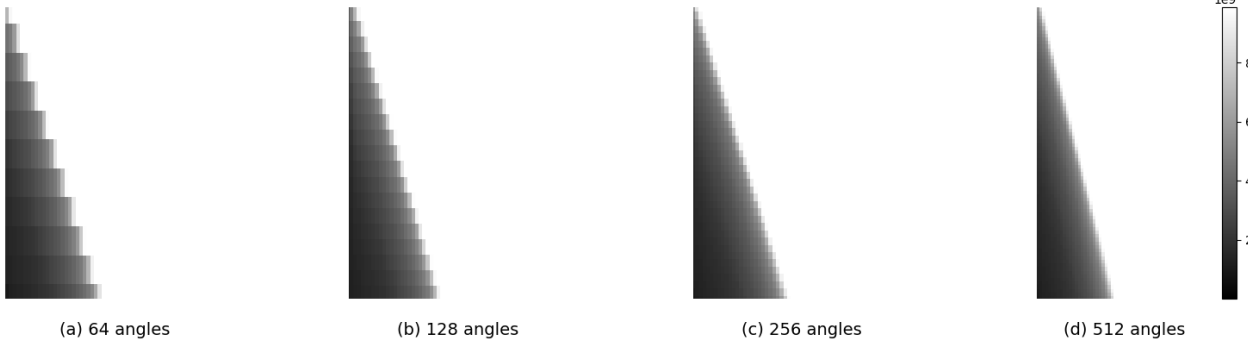

(a) 64 angles   (b) 128 angles   (c) 256 angles   (d) 512 angles

Figure 4: Magnified section of the raw sinogram of a single large titanium hip replacement.

An approximation for the *total attenuation* μ_{tot} along each X-ray beam can be found by assuming the linear attenuation coefficients vary only with material and not photon energy:

$$\mu_{\text{tot}} \equiv \sum_m \mu_{m,E} x_m \approx \sum_m \mu_m x_m = -\log_e \frac{I_{\text{tot}}}{\sum_E I_{0,E}}. \tag{4}$$

The CT detection sinogram is converted to a linear attenuation sinogram by `ct_calibrate`, a function which applies the approximation outlined in eq. (4). The total source beam intensity I_0 is found by a calibration scan, by recording detector values for a phantom consisting of just air. The effect of calibrating the sinogram can be seen in Fig. 5, in which disks of different material were scanned using a 100 kVp ideal source. The sinogram data values corresponding to the disk increase from aluminium to titanium to copper, scaling with the linear attenuation coefficient as expected.

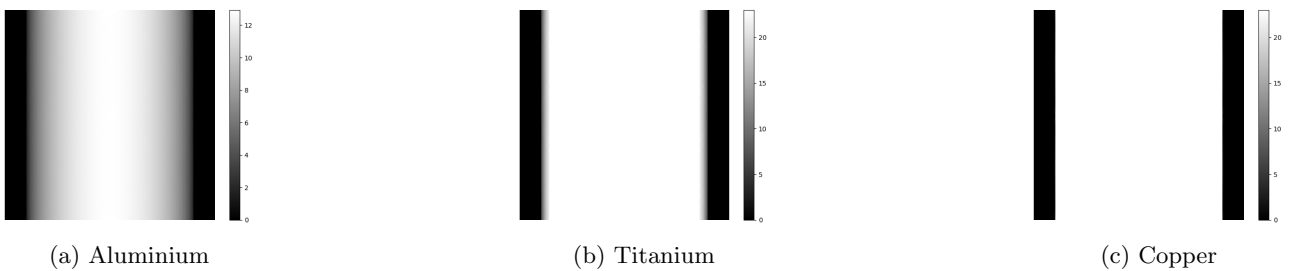(a) Aluminium   (b) Titanium   (c) Copper

Figure 5: Scan of a phantom disk with a 100kVp ideal source for various materials.

Changes to the interpolation method were investigated qualitatively by comparing the calibrated sinograms for a single large titanium hip implant, the results of which are shown in Fig. 6. The two spline interpolation schemes used to produce Fig.s 6b and 6c give much smoother sinograms than that of Fig. 6a, which was generated using nearest neighbour. This highlights the superiority of spline interpolants over nearest neighbour- they yield results closer to that of the ideal sinogram, which would vary continuously in attenuation value.

5

(a) Nearest neighbour

(b) Linear interpolation
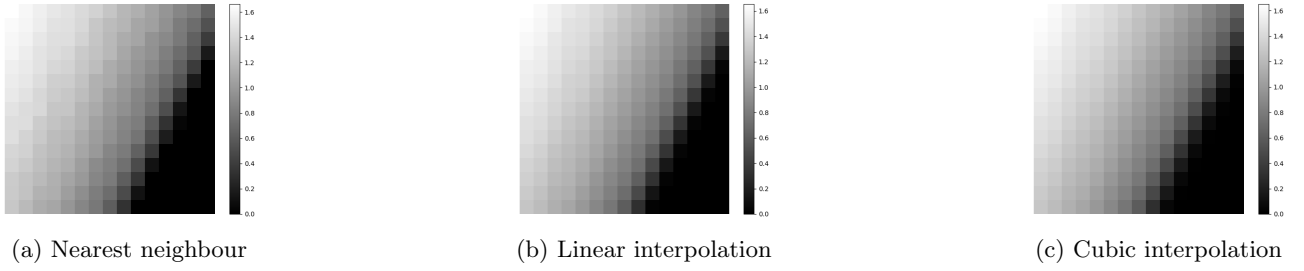

(c) Cubic interpolation

Figure 6: Magnified section of the calibrated sinogram for a single large titanium hip replacement for various interpolation methods, scanned using a 100kVp ideal source.

4   Reconstructing Cross-Sectional Data

Reconstruction is a mathematical procedure used to find the original attenuation distribution from an acquired sinogram, such that a cross-sectional image can be formed. In the case of the CT simulator, this was implemented through *filtered back-projection* (FBP), an analytic reconstruction algorithm which involves convolving the calibrated sinogram with a ramp-filter, known as a *Ram-Lak* filter, prior to *back-projecting*. The Ram-Lak filter gives the optimal spacial resolution in the reconstructed image [1]. Details of FBP and mathematical derivations for the form of the Ram-Lak filter as well as its variants can be found in Section 5 of the project handout.

The process of discretised back-projection is achieved by the `back_project` function. For each projection angle θ, the measured attenuation along a given offset r is divided up equally among the pixels along the measurement beam. The contributions for each pixel are summed over all measured angles to yield the back-projected image. In general, the pixel array will not be aligned with the beam geometry. Hence, pixel data values are found through interpolation of the recorded attenuation data. As with the `ct_scan` function, this was done by calling the SciPy library function `ndimage.map_coordinates`.

A dense point in the phantom can be identified on the back-projected image at the intersection of dense strips from all of the projections, which form a star-shaped pattern [6]. In 2D, this pattern is termed the *point-spread-function* (PSF). The reconstructed image is the original image blurred by the PSF, giving rise to star-shaped artefacts, the formation of which are shown in Fig. 7a. This is a major shortcoming in the back-projection method and is what prevents a perfect reconstruction of the image of the phantom. The issue of blurring is significantly reduced in the convolution stage of FBP: the form of the filter is such that the pattern to be back-projected has additional positive and negative parts. When back-projected and summed with the rest of the filtered and back-projected projections, there is almost complete cancellation of the blurring artefact. The improvement in the reconstruction by the convolution stage can be seen by comparing Fig.s 7b and 7c, which show the reconstructed images for the titanium hip replacement phantom shown in Fig. 14a using back-projection and FBP. In practice, a *raised-cosine* form of the Ram-Lak filter is implemented. This filter is designed to avoid amplification of high-frequency noise components, taking a narrower band than the Ram-Lak filter. However, this comes at the expense of imperfect blur removal, as the filter no longer takes the ideal ramp-filter form.

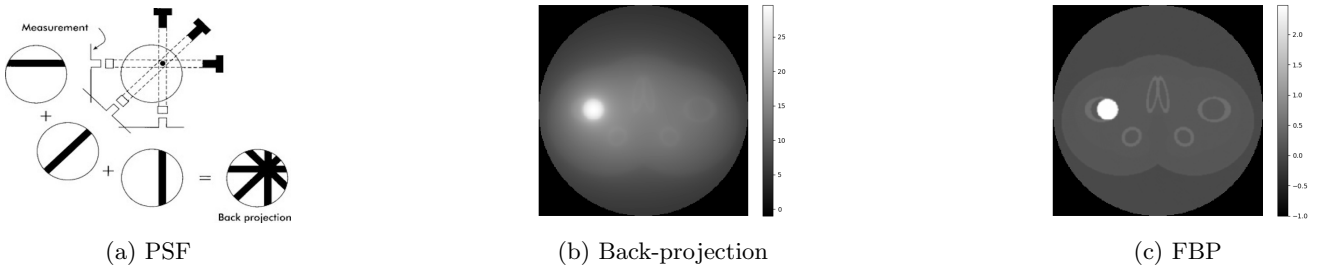(a) PSF

(b) Back-projection

(c) FBP

Figure 7: (a) Formation of the point-spread function (PSF) in back-projection [8]. (b) Reconstructed image using back-projection alone. (c) Filtered back-projection (FBP) using a Ram-Lak filter.

In order to investigate changes to the interpolants, scanning angles and filter on the reconstruction process, three test functions were written. Test 1 provides a direct visual comparison of the original phantom and

reconstructed image by displaying the two side-by-side. Test 2 quantitatively assesses the geometrical accuracy of a reconstructed CT image, by comparing the location of features with the original phantom. The accuracy of the returned linear attenuation coefficients is determined by Test 3. The workings of each test can be found in the `ct_test_example` file in the CT simulator code. Tests 2 and 3 perform 10 and 15 simulations respectively, in which a variety of phantom cases and accuracy thresholds are used. For the purposes of the investigation, the average error from each test was returned to provide an accuracy metric for the configuration of the simulator. When running Test 3, it was not possible to reduce the percentage error in linear attenuation coefficient below 0.3%. This is due to a reconstruction bias error that a zero DC filter gain introduces [13], which is only approximately corrected for by the Ram-Lak filter.

The reconstructed image for a 256 x 256 phantom consisting of a single large titanium hip replacement scanned using a 100 kVp source energy distribution is shown in Fig. 8. The effect of too few projections can be seen clearly in the image reconstructions for 64 and 128 scanning angles, where alternating dark and bright streak artifacts are present in the regions of smallest sampling density. A close inspection of the reconstructed image in Fig. 8c for 256 scanning angles also reveals the presence of such artifacts, albeit on a much smaller scale. The mathematical derivation for the minimum number of parallel rays N_{min} to avoid these streak artifacts is outlined in Buzug (2010), the result of which is $N_{\min} = 2\pi R\nu_M$, where R is the radius of the artifact-free zone of reconstruction and ν_M the maximum spacial frequency in the reconstructed image. To avoid aliasing artifacts, the maximum spacial frequency must be less than half the sampling rate, that is the Nyquist sampling frequency. The constructed simulator is designed to image square phantoms of dimension n cm and `scale` cm per pixel, hence $R = 2n \times$ `scale` and $\nu_M < \frac{1}{2 \times \text{scale}}$, such that $N_{\min} = \frac{\pi n}{2}$. For the 256 x 256 phantom imaged in Fig. 8, $N_{\min} = 403$. This explains why no streak artifacts are present in Fig. 8d, the reconstructed image obtained using 512 angles. A phantom of half the dimension (128 x 128) would only require half the scanning angles (202) to avoid undersampling and the inclusion of streak artifacts.

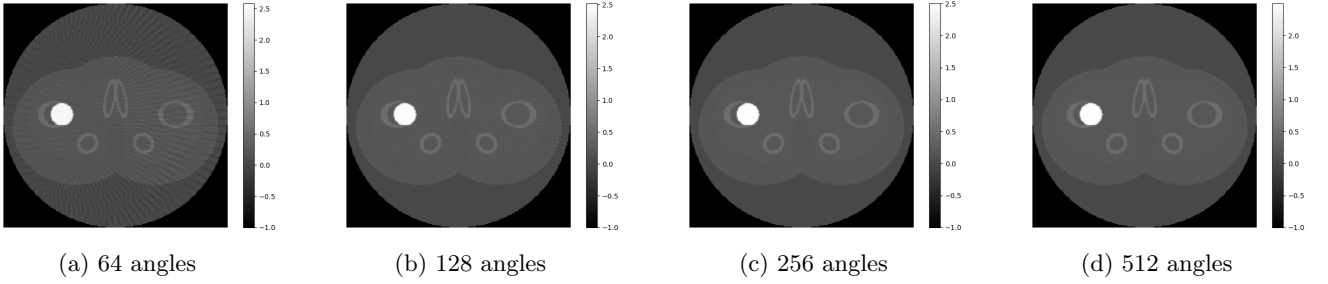| (a) 64 angles | (b) 128 angles | (c) 256 angles | (d) 512 angles |

Figure 8: Reconstructed image of a 256 x 256 phantom consisting of a single large titanium hip replacement for various numbers of scanning angles.

Following this, the effect of the interpolation scheme used in the function `back_project` was investigated by scanning a 256 x 256 single large titanium hip replacement with a 100 kVp ideal source, the results of which are which are shown in Fig. 9. There is significant discrepency between the reconstructed image formed through nearest neighbour and the original phantom. As interpolated pixel intensities take the value of their closest neighbour, the clear divide between regions of bone and soft tissue are lost. These artifacts are reduced as the interpolation order is increased, the bone feature regaining a degree of smoothness and distinction from the soft tissue region. This is expected, as these spline interpolants are G^0 continuous.

(a) Phantom   (b) Nearest neighbour   (c) Linear interpolation   (d) Cubic interpolation
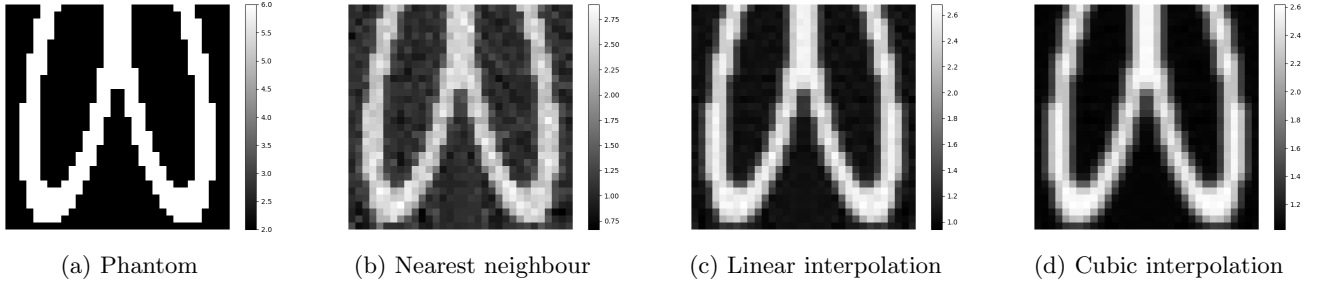
Figure 9: Phantom and reconstructed images of the central bone feature for phantom case 3 using various interpolation schemes. For each scheme, the phantom was scanned using 256 scanning angles and an ideal 100 kVp source energy distribution.

To quantify the change in geometrical accuracy, Tests 2 and 3 were conducted for each of the interpolation schemes. Table 2 shows the returned average errors, which reveal that linear interpolation produced the greatest geometrical accuracy, followed by cubic interpolation and lastly nearest neighbour. The average error in linear attenuation coefficient decreased with order of interpolant, being greatest for nearest neighbour and lowest for cubic. Considering these results in conjunction with those form the `ct_scan` interpolantion investigation, spline interpolants are shown to be favourable over nearest neighbour. The exact order of interpolant is chosen depending on whether geometrical or attenuation accuracy is of greater importance.

Table 2: Average errors for Tests 2 and 3 for each back-projection interpolation method.

Average error (%)	NN	Linear	Cubic
Test 2	28.67	26.74	27.22
Test 3	1.09	0.42	0.33

Finally, changes to the Ram-Lak filter were investigated, namely by multiplying the filter by a cosine raised to the power of the variable `alpha` to produce raised-cosine filter frequency responses. The impulse response of the Ram-Lak filter for a 256 x 256 array is shown in Fig. 10b. The figure confirms than an input impulse is mapped to the spacial form of the filter function, as outlined in [13].

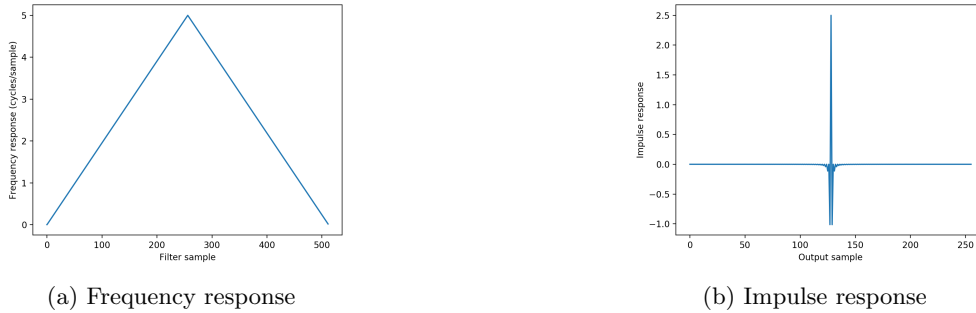(a) Frequency response   (b) Impulse response

Figure 10: Ramp filter response. (a) Python implementation of the Ram-Lak filter in the frequency domain. (b) Impulse response of the filter.

The results of varying `alpha` to take values of 0, 0.01, 0.05, 0.1 and 0.5 are recorded in Table 4. For this set of parameters, the greatest geometrical accuracy was obtained for `alpha` = 0.05, and the greatest linear attenuation coefficient accuracy for `alpha` = 0.01. Increasing `alpha` produces a filter which attenuates noise to a greater degree, however this is at the expense of a greater deviation from the ideal Ram-Lak filter form, thus impacting the spacial resolution of the reconstructed image.

Table 4: Average errors for Tests 2 and 3 for various filter parameters.

Average Error (%)	Alpha				
	0	0.01	0.05	0.1	0.5
Test 2	26.80	26.75	25.67	27.48	30.51
Test 3	0.48	0.48	0.45	0.16	0.32

5 CT Noise and Current

The CT simulator was extended to cover the effects of noise in the scanning process, such that the reconstructed image varied with the radiation dose. The X-ray source intensities were assumed to follow a Poisson distribution, and the probability of each photon interacting with an atom constant. Taking each interaction event to be independent of any other, the number of atom interactions follows a Bernoulli distribution. Since a Poisson random variable 'input' to a Bernoulli distribution yields another Poisson random variable, the source-interaction pair is again a Poisson random variable, with intensity scaled by the probability of detection [3]. In this case, the mean of the distribution is given by eq. (1). The amount of scatter noise scales with radiation dose, as higher doses give a greater number of source photons. Also considered was the effect of background radiation, which contributes a fixed additive term to the detected intensities.

The source distribution was implemented by modifying the `attenuate` function such that the input energies were generated under the NumPy library Poisson distribution. Likewise, the proportion of transmitted, background and scattered photons were found from Poisson distributions in `ct_detect`. The amount of background and scatter noise were found through a trial and improvement process, in which the proportions of each were varied until realistic reconstructions were obtained for doses in the order of ~ 100 mAs, a typical dose for the pelvic CT scan of an average sized person [5]. The effect of noise on the reconstruction can be seen by comparing Fig.s 11a and 11b.

(a) No noise   (b) 100 mAs dose, 256 x 256 phantom   (c) 200 mAs dose, 256 x 256 phantom   (d) 200 mAs dose, 512 x 512 phantom
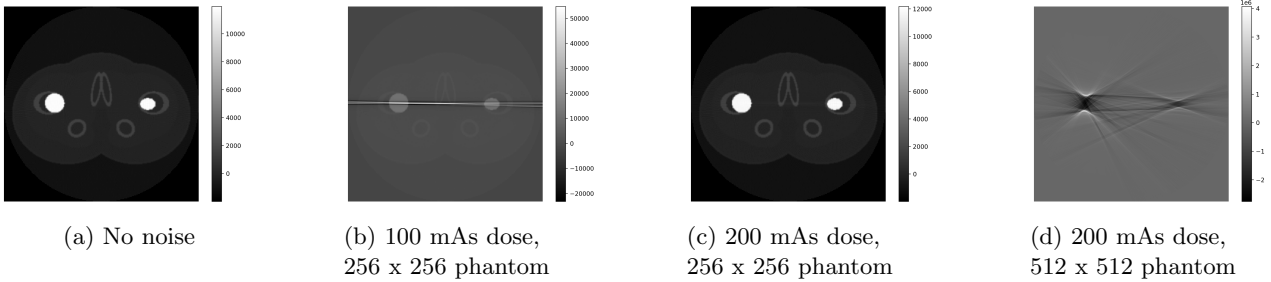
Figure 11: Comparison of reconstructed images with the implementation of noise. (a), (b) and (c) show scans for a 256 x 256 phantom with varying doses, whereas (d) is a 512 x 512 phantom.

Fig.s 11b and 11c show the improvement in SNR in the reconstructed image by increasing the dose from 100 mAs to 200 mAs for a 256 x 256 phantom. Scanning larger phantoms, such as the 512 x 512 phantom in Fig 11d, requires higher doses to produce CT images with acceptable SNRs, as bigger sizes attenuate more [12]. Sections of highly attenuating material, such as the titanium hip replacements in Fig. 12, introduce significant streak artifacts, which swamp the image with noise unless higher doses are used.

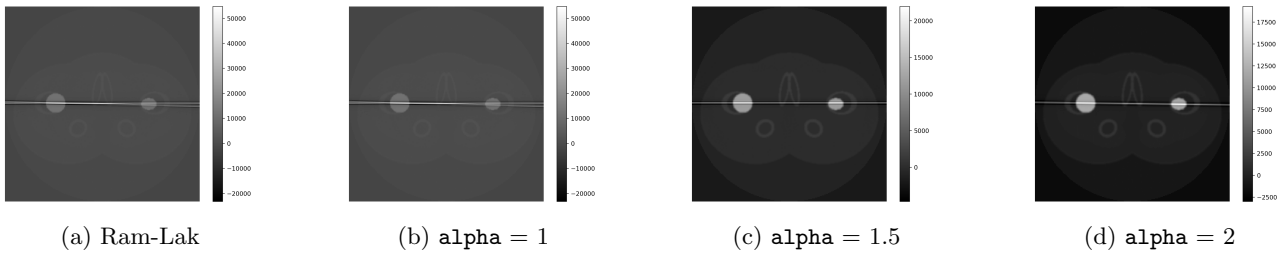| (a) Ram-Lak | (b) `alpha = 1` | (c) `alpha = 1.5` | (d) `alpha = 2` |

Figure 12: Reconstructed image for various exponents of the raised-cosine filter.

Using a raised-cosine filter, which more greatly attenuates noise than a Ram-Lak filter, yields improvements in the SNR of the reconstructed image. A large amount of the background and scatter noise can be reduced by setting `alpha > 1`, such as in Fig.s 12c and 12d, however the streak effects caused by very attenuating materials remain. The smallest value of `alpha` which reduces noise to an acceptable degree should be used, to minimise the impact on spacial resolution.

6 Conclusion

A Python simulation of the CT process was developed and a number of parameters and properties investigated.

There is a minimum number of angles which must be scanned over to avoid streak artifacts. In both data acquisition and reconstruction, spline interpolants proved to be more beneficial than nearest neighbour in achieving smooth reconstructions. The filter form in the FBP process is chosen as a trade-off between the attenuation of noise and the spacial resoution of the reconstructed image. Finally, the CT simulator was extended to incorporate the effects of transmission, background and scatter noise. The effects of noise are more prevalent at low doses, with larger subjects requiring higher doses for adequate image reconstruction. The impacts of noise from low doses can be suppressed by setting the exponent of the raised-cosine filter above 1 can, however streak artifacts from highly attenuating materials remain.

References

[1] Thorsten Buzug. *Computed Tomography- From Photon Statistics to Modern Cone-Beam CT*. Springer, Berlin, 2010.

[2] Guillermo A. Cervantes. Radiographic quality. In *Technical Fundamentals of Radiology and CT*, 2053-2563, pages 2–1 to 2–11. IOP Publishing, 2016.

[3] Charles Epstein. *Introduction to the Mathematics of Medical Imaging*. Society for Industrial and Applied Mathematics (SIAM, 3600 Market Street, Floor 6, Philadelphia, PA 19104), Philadelphia, Pa, 2008.

[4] Carolyn A. MacDonald. *An Introduction to X-Ray Physics, Optics, and Applications*. Princeton University Press, 2017.

[5] J. R. Mayo, T. E. Hartman, K. S. Lee, S. L. Primack, S. Vedal, and N. L. Müller. CT of the chest: minimal tube current required for good image quality with the least radiation dose. *American Journal of Roentgenology*, 164(3):603–607, Mar 1995.

[6] William W. Orrison and John A. Sanders. *Clinical Brain Imaging: Computerized Axial Tomography and Magnetic Resonance Imaging*. Mosby-Year Book, Inc., 1995.

[7] Rachel A. Powsner, Matthew R. Palmer, and Edward R. Powsner. *Essentials of Nuclear Medicine Physics and Instrumentation*. John Wiley & Sons, Incorporated, Somerset, UNITED STATES, 2013.

[8] Philip Saia. *Clinical Gynecologic Oncology*. Elsevier/Saunders, Philadelphia, PA, 2012.

[9] J. Anthony Seibert and John M. Boone. X-ray imaging physics for nuclear medicine technologists. part 2: X-ray interactions and image formation. *Journal of Nuclear Medicine Technology*, 33(1):3–18, 2005.

[10] Joseph Selman. *The Fundamentals of Imaging Physics and Radiobiology.*, volume 9th ed. Charles C Thomas, 2000.

[11] Perry Sprawls. *Physical Principles of Medical Imaging.* Medical Physics Pub, Madison, Wis, 1995.

[12] Paul Suetens. *Fundamentals of Medical Imaging.* Cambridge University Press, 3 edition, 2017.

[13] G. L. Zeng. Revisit of the ramp filter. In *2014 IEEE Nuclear Science Symposium and Medical Imaging Conference (NSS/MIC)*, pages 1–6, 2014.

7 Appendix

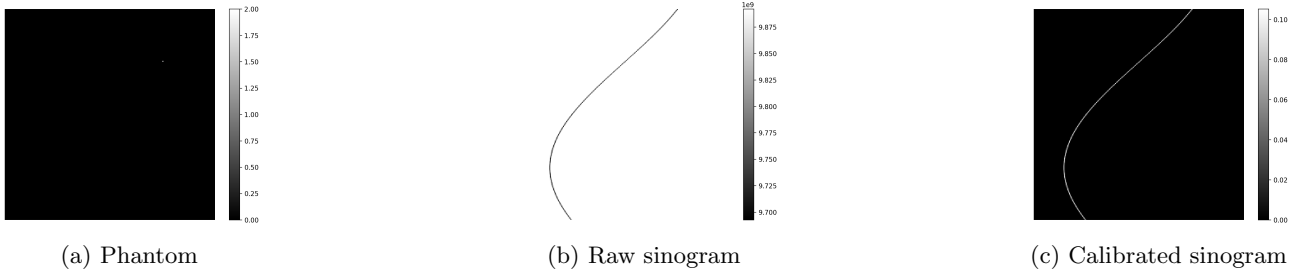(a) Phantom   (b) Raw sinogram   (c) Calibrated sinogram

Figure 13: Scan of a soft tissue impulse at the centre of the first quadrant with a 100kVp ideal source. The sinusoidal distribution obtained is what gives the sinogram its name.

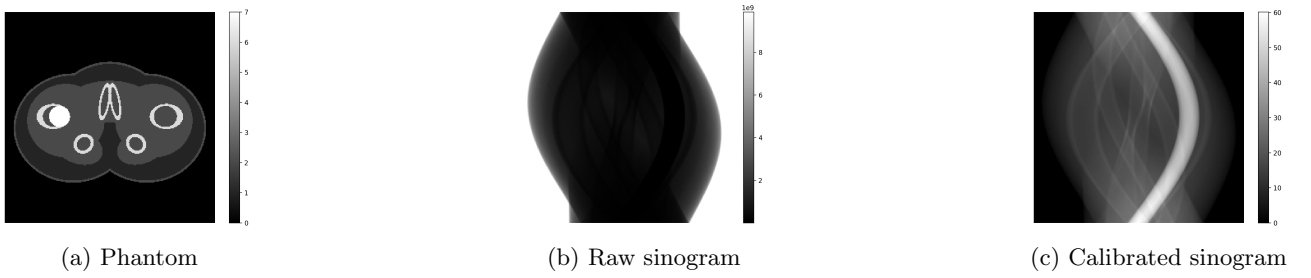(a) Phantom   (b) Raw sinogram   (c) Calibrated sinogram

Figure 14: Scan of a single large titanium hip replacement with a 100kVp ideal source.